

Odin observations of water in molecular outflows and shocks^{★,★★}

P. Bjerkeli¹, R. Liseau¹, M. Olberg^{1,2}, E. Falgarone³, U. Frisk⁴, Å. Hjalmarsen¹, A. Klotz⁵, B. Larsson⁶, A.O.H. Olofsson^{7,1}, G. Olofsson⁶, I. Ristorcelli⁸, and Aa. Sandqvist⁶

¹ Onsala Space Observatory, Chalmers University of Technology, SE-439 92 Onsala, Sweden

² SRON, Landleven 12, P.O.Box 800, NL-9700 AV Groningen, The Netherlands

³ Laboratoire de Radioastronomie - LERMA, Ecole Normale Supérieure, 24 rue Lhomond, 75231 Paris Cedex 05, France

⁴ Swedish Space Corporation, PO Box 4207, SE-171 04 Solna, Sweden

⁵ CESR, Observatoire Midi-Pyrénées (CNRS-UPS), Université de Toulouse, BP 4346, 31028 Toulouse Cedex 04, France

⁶ Stockholm Observatory, Stockholm University, AlbaNova University Center, SE-106 91 Stockholm, Sweden

⁷ GEPI, Observatoire de Paris, CNRS, 5 Place Jules Janssen, 92195 Meudon, France

⁸ CESR, 9 avenue du Colonel Roche, BP 4346, 31029 Toulouse, France

Preprint online version: June 30, 2021

ABSTRACT

Aims. We investigate the *ortho*-water abundance in outflows and shocks in order to improve our knowledge of shock chemistry and of the physics behind molecular outflows.

Methods. We have used the Odin space observatory to observe the H₂O(1₁₀ – 1₀₁) line. We obtain strip maps and single pointings of 13 outflows and two supernova remnants where we report detections for eight sources. We have used RADEX to compute the beam averaged abundances of *o*-H₂O relative to H₂. In the case of non-detection, we derive upper limits on the abundance.

Results. Observations of CO emission from the literature show that the volume density of H₂ can vary to a large extent, a parameter that puts severe uncertainties on the derived abundances. Our analysis shows a wide range of abundances reflecting the degree to which shock chemistry is affecting the formation and destruction of water. We also compare our results with recent results from the SWAS team.

Conclusions. Elevated abundances of *ortho*-water are found in several sources. The abundance reaches values as high as what would be expected from a theoretical C-type shock where all oxygen, not in the form of CO, is converted to water. However, the high abundances we derive could also be due to the low densities (derived from CO observations) that we assume. The water emission may in reality stem from high density regions much smaller than the Odin beam. We do not find any relationship between the abundance and the mass loss rate. On the other hand, there is a relation between the derived water abundance and the observed maximum outflow velocity.

Key words. interstellar medium: jets and outflows – interstellar medium: molecules – interstellar medium: supernova remnants – stars: pre-main-sequence

1. Introduction

Deeply embedded Class 0 stellar systems are observed to be associated with high velocity bipolar outflows (see e.g. Snell et al. 1980) which are believed to play an important role when stars are formed. During the phase when material is accreted onto the newborn star through the circumstellar disk, outflows are responsible for a necessary re-distribution of angular momentum. The specific angular momentum of the infalling material must at some point decrease to allow the final collapse. Although the basic theoretical concepts can be understood, there is still a great observational need to get further knowledge about the engine of these flows. Different models describing the driving mechanisms have been proposed and for that reason it is important to derive

abundances of different species in order to distinguish between different physical scenarios. In this context, water is interesting in the sense that it is strongly affected by the presence of different types of shocks. At low temperatures, water is formed through a series of ion molecule reactions. This process is relatively slow and enhanced water abundances are thus not expected. At higher temperatures, the activation barrier for neutral-neutral reactions is reached, and for that reason water can be formed in a much more efficient way. Such elevated temperatures are reached in low velocity shocks, where the shock is smoothed by friction between ions and neutrals, called continuous shocks (see e.g. Bergin et al. 1998). Here, H₂ is prevented from destruction and enhanced water abundances are expected. In this scenario, water is not only formed through reactions with oxygen but can also be released from its frozen state on dust grains (Kaufman & Neufeld 1996). In the discontinuous type of shock (jump shock), H₂ is instead dissociated and water formation is prevented. The detection of water is aggravated by the difficulty of observing from ground based observatories. Prior to the launch of Odin (Nordh et al. 2003; Hjalmarsen et al. 2003), two space born observatories capable of detecting water have been in operation, the *Infrared Space Observatory* (ISO) (Kessler et al. 1996) and the *Submillimeter Wave Astronomy Satellite* (SWAS) (Melnick

Send offprint requests to:

P. Bjerkeli, e-mail: per.bjerkeli@chalmers.se

* Odin is a Swedish-led satellite project funded jointly by the Swedish National Space Board (SNSB), the Canadian Space Agency (CSA), the National Technology Agency of Finland (Tekes) and Centre National d'Etude Spatiale (CNES).

** The Swedish ESO Submillimetre Telescope (SEST) located at La Silla, Chile was funded by the Swedish Research Council (VR) and the European Southern Observatory. It was decommissioned in 2003.

et al. 2000). The latter of these two also had the ability to observe the ground state transition of *o*-H₂O although the beam size was larger (3.3 × 4.5 elliptical compared to 2.1 circular for Odin). Water abundances derived from ISO data are in general higher than those derived from SWAS data. This discrepancy is addressed in the paper by Benedettini et al. (2002). In 2003, the *Spitzer Space Telescope*, capable of detecting hot water was launched (Werner et al. 2004).

In this paper, H₂O(1₁₀ – 1₀₁) observations of 13 outflows and two supernova remnants are discussed. Shocks from supernova explosions have similar effect on the chemical conditions as molecular outflows. The different sources are discussed in Section (4.2) and summarized in Table 1 and 2. Table 3 includes other outflows observed by Odin that have already been investigated by other authors or are in preparation for publication (W3, Orion KL, ε Cha-MMS1, IRAS 16293-2422, S140 and VLA1623). The analysis carried out in these papers is however different from the analysis made in the present paper. Similar observations as the ones discussed here have recently been presented by the SWAS team (Franklin et al. 2008). For that reason we make a brief comparison of the results for common sources.

2. Observations and reductions

2.1. H₂O observations

All *o*-H₂O observations were made with the Odin space observatory between 2002 and 2007 (see Table 1). Each revolution of 96 minutes allows for 61 minutes of observations, whereas the source is occulted by the Earth for the remaining 35 minutes. The occultations allow for frequency calibration using atmospheric spectral lines. At the wavelength of the *ortho*-water ground state transition, the 1.1 m Gregorian telescope has a circular beam with Full Width Half Maximum (FWHM) of 126'' (Frisk et al. 2003). The main beam efficiency is close to 90 % as measured from Jupiter mappings (Hjalmarson et al. 2003). The main observing mode was sky switching, where simultaneous reference measurements from an unfocused 4.4 FWHM sky beam were acquired. Position switching, where the entire spacecraft is re-orientated in order to obtain a reference spectrum, was the method of observation for a smaller number of targets. Three different spectrometers were used. Two of these are autocorrelators (AC1, AC2) and the third one is an acousto-optical spectrometer (AOS). The AOS has a channel spacing of 620 kHz (0.33 km s⁻¹ at 557 GHz), while the autocorrelators can be used in different modes. The majority of the data have a reconstructed pointing offset less than 20''. The data processing and calibration is described in detail by Olberg et al. (2003).

3. Results

The baseline-subtracted H₂O spectra for the 15 previously not published sources are presented in the right column of Figures B.1 - B.4. All spectra are smoothed to a resolution of 0.5 km s⁻¹. The velocity interval has been chosen in order to emphasize the line profiles. In the left column, the calibrated raw data are plotted for comparison. These spectra have their baselines subtracted using a zeroth order polynomial.

4. Discussion

4.1. Densities, temperatures and radiative transfer analysis

In this paper we derive the beam averaged *ortho*-water abundance. The beam size is however likely to be larger than the

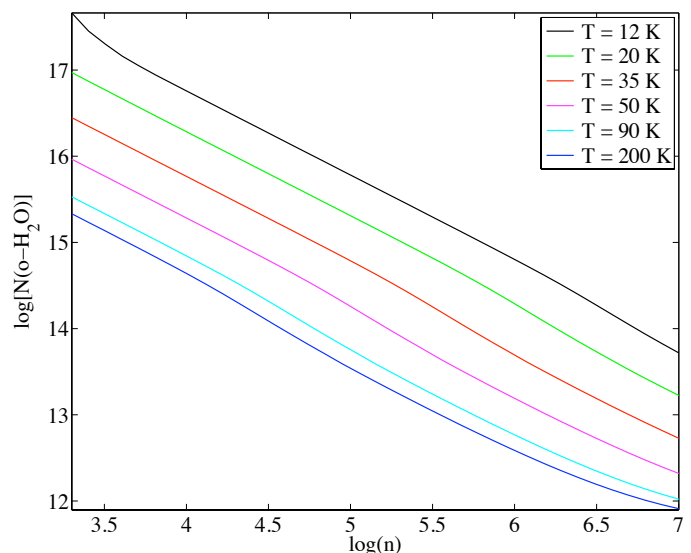


Fig. 1. The derived *o*-H₂O column density as a function of volume density for different temperatures. The line intensity for this test case has been set to 0.1 K while the line width has been set to 10 km s⁻¹.

emitting regions for several of the sources that are analyzed. In order to do this, we use RADEX¹ (van der Tak et al. 2007). It is a publically available code that uses the method of mean escape probability for the radiative transfer. For interstellar gas at relatively low temperatures and densities ($\ll 10^8$ cm⁻³) water excitation will be subthermal and the emission be on the linear part of the curve of growth, i.e. even an optically thick line will behave as being effectively optically thin (Linke et al. 1977; Snell et al. 2000). For an effectively optically thin line, the result of a radiative transfer code like RADEX is essentially the same as that of the analytical expression for a collisionally excited transition

$$F = hv \frac{\Omega}{4\pi} X_{\text{mol}} N(\text{H}_2) \gamma_{\text{lu}} n(\text{H}_2) \frac{\frac{\beta_c n_c}{n(\text{H}_2)}}{\frac{\beta_c n_c}{n(\text{H}_2)} + \frac{\gamma_{\text{ul}}}{\gamma_{\text{ul}}} + 1} \quad (1)$$

(Liseau & Olofsson 1999). F is the integrated line flux, γ_{lu} and γ_{ul} are the upward and downward collision coefficients, n_c is the critical density and β_c is the photon escape probability. The molecular datafiles that are used by RADEX are taken from the Leiden Atomic and Molecular Database (LAMDA)². Here, the collision rates between *o*-H₂O and H₂ have been retrieved from Phillips et al. (1996), Dubernet & Grosjean (2002) and Faure et al. (2007). Recently, new rate coefficients of *o*-H₂O with *p*-H₂ have been published by Dubernet et al. (2009). According to the results presented in this paper (their Figure 8), collision rates used in RADEX should not differ by more than a factor of three in the temperature regime below 40 K. The ortho to para ratio of H₂ is in RADEX assumed to be thermal. As input parameters, the line intensity, line width, kinetic temperature and volume density of the observed gas must be supplied. The difficulty in obtaining good estimates for the two latter parameters has to be kept in mind. In Figure 1, we plot the *o*-H₂O column density as a function of volume density for a test case. The line intensity has been set to 0.1 K and the linewidth to 10 km s⁻¹. From this figure, it is clear that the derived abundances are very uncertain when the kinetic temperatures are low.

¹ <http://www.strw.leidenuniv.nl/moldata/radex.html>

² <http://www.strw.leidenuniv.nl/moldata/>

Table 1. Observation log for the sources analyzed in this paper.

Source	$\alpha(2000)$ (hr:min:sec)	$\delta(2000)$ (deg:min:sec)	Distance (pc)	Backend	Date (YYMMDD)	t_{int} (hr)
L1448	03:25:38.8	+30:44:05	250	AOS	060722 - 060813	38
HH 211	03:43:56.5	+32:00:50	315	AOS	070119 - 070209	22
L1551	04:31:34.1	+18:08:05	140	AC2	020208 - 020213	12
IC443-G	06:16:43.4	+22:32:24	1500	AOS	020319 - 020321	5
TW Hya	11:01:51.9	-34:42:17	56	AOS	031118 - 031204	18
ϵ Cha IN	11:09:54.6	-76:34 24	150	AC2	031205 - 031212	11
Sa136 (BHR71)	12:01:37.0	-65:08:54	200	AOS	060528 - 060721	41
HH54 B	12:55:50.3	-76:56:23	200	AC2	050502 - 050620	10
G327.3-0.6	15:53:08.7	-54:37:01	2900	AC2	030731 - 030807	11
NGC6334I	17:20:53.4	-35:47:02	1700	AC1	010926 - 010927	2
Ser SMM1	18:29:49.8	+01:15:21	310	AC2	041026 - 041031	9
3C391 BML	18:49:22.0	-00:57:22	8000	AC2	041101 - 041106	14
B335	19:37:01.0	+07:34:11	250	AC2	031024 - 031101	7
L1157	20:39:06.4	+68:02:13	250	AC2/AOS	051129 - 060127	119
NGC7538 IRS1	23:13:46.8	+61:28:10	2700	AOS	011214 - 011214	1

In this study, the temperature is taken from the literature while the volume density is inferred from CO observations carried out by others. These two parameters are however not expected to have constant values across the large Odin beam due to the quite complex morphology of molecular outflows. For all the sources, we only include the cosmic microwave background as a radiation field. For simplicity we have chosen the line intensity to be equal to the peak value while the line width is taken as the width of the line at 50 % of this value. The output column density of *ortho*-water is then used to derive the abundance relative to molecular hydrogen, $X(o\text{-H}_2\text{O}) = N(o\text{-H}_2\text{O})/N(\text{H}_2)$.

A widely recognized method to obtain the column density for H_2 is to measure the CO abundance assuming a constant universal ratio, e.g. $[\text{CO}/\text{H}_2] = 10^{-4}$ (see e.g. Dickman 1978). In this paper we use this method where it is feasible (different methods are used for TW Hya and 3C391 BML). Volume densities and beam averaged column densities are estimated from literature data assuming cylindrical geometry and a mean molecular weight $\mu = 2.4$. No correction for inclination is made. The inferred volume densities (Method 1) should be considered as lower limits for two reasons. First, the size of the water emitting regions is poorly known. These regions may very well be smaller than the CO emitting regions, potentially resulting in a higher average density. Secondly, shocks, if present, will compress the gas even further. For some of the sources, there are estimates of the volume density, given in the literature, that are significantly higher than the ones used in this paper. In these cases we also estimate an alternative *ortho*-water abundance (Method 2).

Table 2 includes the measured integrated intensity over the observed lines and the derived water abundance. The integrated intensity is measured over the entire line including the central region as well as the outflow wings. Excepted are those outflow sources, for which strong self absorption can be seen (e.g. L1157, Ser SMM1). For these objects, the integrated intensity has been measured for the red and the blue wings separately. For sources with no detection, we set a 3σ upper limit on the integrated intensity in a velocity interval of 10 km s^{-1} (except for TW Hya, where a linewidth of 1 km s^{-1} has been used).

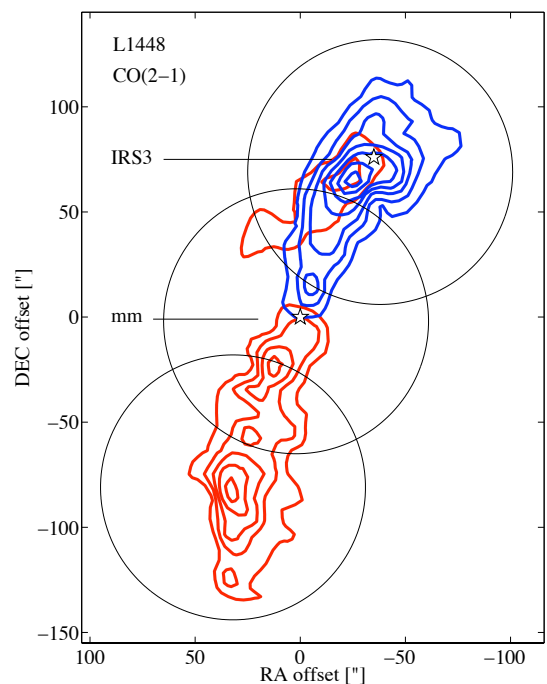


Fig. 2. The three positions observed by Odin are shown overlaid on a CO (2-1) map of L1448 (Bachiller et al. 1995). The circles correspond to the Odin beam at 557 GHz. Coordinate offsets are given with respect to L1448-mm: $\alpha_{2000} = 03:25:38.8$, $\delta_{2000} = 30:44:05.0$. The positions of L1448-mm and L1448 IRS3 are indicated by star symbols.

4.2. Notes on individual sources

4.2.1. L1448

L1448 is a dark cloud in the constellation of Perseus at the distance of 250 pc (Enoch et al. 2006). The large, highly collimated outflow originating from L1448-mm shows enhanced emission from SiO in both lobes (Nisini et al. 2007). Franklin et al. (2008) report *o*- H_2O abundances of $X(o\text{-H}_2\text{O}) = 1.5 \times 10^{-6}$

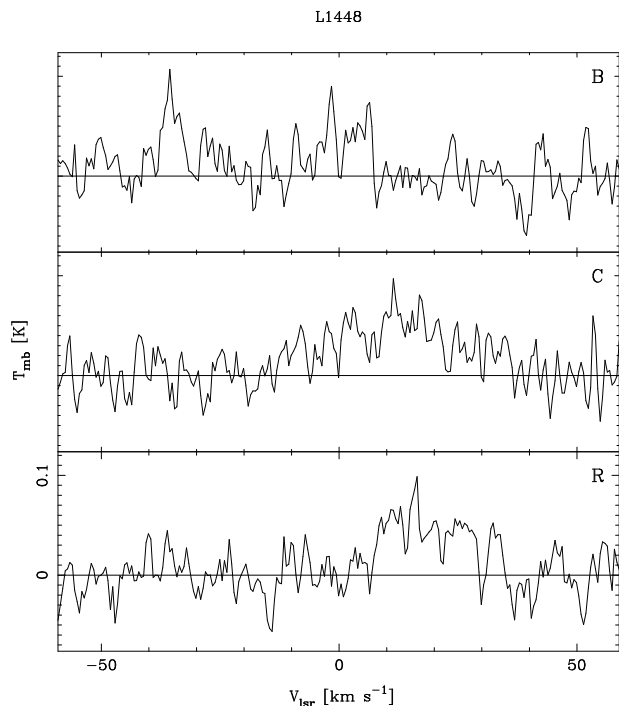


Fig. 3. L1448 spectra. The positions are listed in Table 2 and shown in Figure 2. A letter in the upper right corner indicates in which part of the flow the spectra have been collected (R=red, B=blue and C=center). The spectra have been baseline subtracted and smoothed to a resolution of 0.5 km s^{-1} .

in the blue wing and $X(o\text{-H}_2\text{O}) = 3.7 \times 10^{-6}$ in the red wing. We report observations in three positions across the structure, where the northern position also covers the outflow from L1448 IRS3. The possible detections in both lobes can, due to instabilities in the baselines, only be classified as likely. There is also a tentative detection of a bullet feature in the northern position at $v_{\text{lsr}} \sim +35 \text{ km s}^{-1}$ and we note that this observation is consistent with the high speed CO bullet B3 reported by Bachiller et al. (1990). However, the preliminary analysis of HCO^+ data, recently taken at the Onsala Space Observatory, does not reveal any emission at this velocity. Mass loss rates of $\dot{M}_{\text{loss}} = 4.6 \times 10^{-6} M_{\odot} \text{ yr}^{-1}$ for L1448-mm and $\dot{M}_{\text{loss}} = 1.1 \times 10^{-6} M_{\odot} \text{ yr}^{-1}$ for L1448 IRS3 were reported by Ceccarelli et al. (1997) based on CO observations carried out by (Bachiller et al. 1990). $N(\text{H}_2) = 6 \times 10^{19} \text{ cm}^{-2}$ and $n(\text{H}_2) = 1 \times 10^3 \text{ cm}^{-3}$ are inferred from mass and size estimates reported by the same authors. We assume the width of the flow to be $40''$. Taking the gas temperature to be $T = 37 \text{ K}$ for all positions (Bachiller et al. 1995, dust temperature towards L1448-mm) we derive *ortho*-water abundances between 6×10^{-4} and 2×10^{-3} in the outflow. Using the higher volume density ($\sim 10^4$) estimated by Bachiller et al. (1990), we derive *ortho*-water abundances between 1×10^{-4} and 3×10^{-4} .

4.2.2. HH211

The Herbig-Haro jet HH211 is also located in Perseus, 315 pc away (Herbig 1998). It was observed in three different positions enclosing the relatively small outflow. The central and northern beams contain the HH211-mm region. We use the mass estimates from Gueth & Guilloteau (1999) as the base for our inferred volume densities, $n(\text{H}_2) = 1 \times 10^4 \text{ cm}^{-3}$ and column densities, $N(\text{H}_2) = 4 \times 10^{19} \text{ cm}^{-2}$ in all three positions. The size of the outflow is taken to be $90'' \times 10''$. The temperature in the clumps

of the IC348 region varies between 12 K close to the centers and 20 – 30 K at the edges (Bachiller et al. 1987). Assuming a temperature $T = 12 \text{ K}$ we derive upper limits of $X(o\text{-H}_2\text{O}) < 8 \times 10^{-4}$ at the central position and $X(o\text{-H}_2\text{O}) < (1 - 2) \times 10^{-3}$ in the outflow. A temperature, $T = 30 \text{ K}$, would lower these upper limits by almost a factor of ten. The two-sided mass loss rate was estimated by Lee et al. (2007) to be $\dot{M}_{\text{loss}} \sim (0.7 - 2.8) \times 10^{-6} M_{\odot} \text{ yr}^{-1}$.

4.2.3. L1551

L1551 is probably one of the most rigorously studied molecular outflows. The main source L1551 IRS5 is located at the distance of 140 pc in the Taurus-Auriga cloud complex (Kenyon et al. 1994). The mass loss rate is in the range $8 \times 10^{-7} < \dot{M}_{\text{loss}} < 2 \times 10^{-6} M_{\odot} \text{ yr}^{-1}$ (Liseau et al. 2005, and references therein). In this paper we use the mass estimate from CO observations provided by Stojimirović et al. (2006) to calculate the volume density and column density to $n(\text{H}_2) = 3 \times 10^3 \text{ cm}^{-3}$ and $N(\text{H}_2) = 1 \times 10^{21} \text{ cm}^{-2}$, respectively. These authors estimate the mass of the outflow to be $7.2 M_{\odot}$ and we estimate the size of the outflow to $1.3 \times 0.2 \text{ pc}$. Assuming a kinetic temperature of 20 K we give upper limits on the *ortho*-water abundance in three positions across the outflow. We obtain upper limits, ranging from $X(o\text{-H}_2\text{O}) < 8 \times 10^{-5}$ to $X(o\text{-H}_2\text{O}) < 2 \times 10^{-4}$.

4.2.4. TW Hya

At the distance of 56 pc (Qi et al. 2008), TW Hya is the most nearby known T Tauri star. Its accretion disk of size $7''$ is seen essentially face-on and is point-like to Odin, i.e. particularly for any H_2O emission region, the beam filling factor would presumably be $\ll 3 \times 10^{-3}$. In our sample, the object has the lowest mass loss rate, viz. $10^{-12 \text{ to } -11} \leq \dot{M}_{\text{loss}} < 7 \times 10^{-10} M_{\odot} \text{ yr}^{-1}$ (Dupree et al. 2005; Lamzin et al. 2004, respectively), and with an age of about 10 Myr (de la Reza et al. 2006), it is likely also the oldest. Herczeg et al. (2004) report the detection of $L\alpha$ -excited H_2 , with an $N(\text{H}_2) = 3 \times 10^{18} \text{ cm}^{-2}$, which appears accurate to within an order of magnitude. This value refers to the innermost disk regions. In the outer disk, CO and other trace molecules, including their isotopic and/or deuterated forms, have also been detected (Kastner et al. 1997; van Zadelhoff et al. 2001; Qi et al. 2008). In the HCN forming regions, the densities are determined to be $10^6 - 10^8 \text{ cm}^{-3}$ (van Zadelhoff et al. 2001). From intermediate J -transitions of CO, these authors estimated temperatures to be in the range $40 \leq T < 150 \text{ K}$.

Not entirely unexpected, Odin did not detect the H_2O 557 GHz line³. For representative disk parameters and a line width of $< 1 \text{ km s}^{-1}$, the rms of 14 mK would imply an abundance, $X(o\text{-H}_2\text{O}) < 1 \times 10^{-8}$. For the modeling we have used a temperature of 40 K. However, increasing this parameter to 150 K will not decrease the derived upper limit by more than 20%.

4.2.5. ϵ Cha I N

The star forming cloud Chamaeleon I is located at a distance of 150 pc (Knude & Hog 1998). From the estimated age ($3.8 \times 10^4 \text{ yr}$), mass ($0.21 M_{\odot}$) and maximum velocity ($\sim 6 \text{ km s}^{-1}$) reported by Mattila et al. (1989), we obtain a mass loss rate, $\dot{M}_{\text{loss}} =$

³ Taking the difference in beam sizes into account, the Odin data are only a slight improvement over those obtained with SWAS (E. Bergin and R. Plume, private communication).

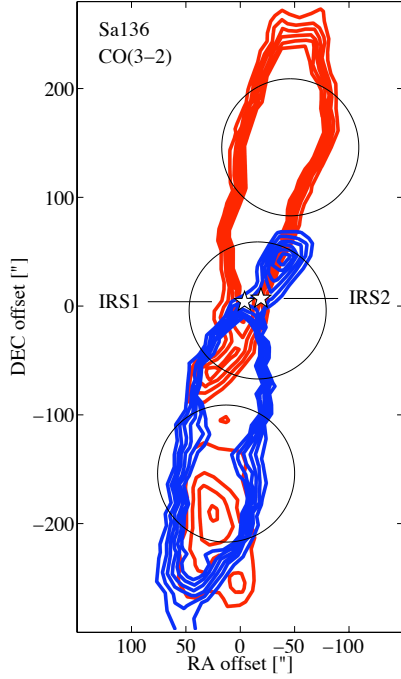


Fig. 4. The three positions observed by Odin are shown overlaid on a CO (3-2) map of Sa136 (Parise et al. 2006). The circles correspond to the Odin beam at 557 GHz. Coordinate offsets are given with respect to: $\alpha_{2000} = 12:01:37.0$, $\delta_{2000} = -65:08:53.5$. The positions of the sources IRS1 and IRS2 are indicated with star symbols.

$3.3 \times 10^{-7} M_{\odot} \text{ yr}^{-1}$. The velocity of the wind is assumed to be 100 km s^{-1} . We estimate $N(\text{H}_2) = 4 \times 10^{20} \text{ cm}^{-2}$ and $n(\text{H}_2) = 2 \times 10^3 \text{ cm}^{-3}$ from CO observations carried out by the same authors. The width of the flow is approximately 0.1 pc. Adopting the temperature 50 K, given by Henning et al. (1993), we obtain an upper limit, $X(o\text{-H}_2\text{O}) < 3 \times 10^{-5}$.

4.2.6. Sa136 (BHR71)

The Sa136 Bok globule outflows (Sandqvist 1977), at about 200 pc distance, are driven by a binary protostellar system. The secondary CO outflow driven by IRS 2 is more compact (Bourke 2001) than the larger outflow driven by IRS 1.

Taking the column density measurements made by Parise et al. (2006), assuming a $[\text{CO}/\text{H}_2]$ ratio of 10^{-4} we obtain $N(\text{H}_2) = 1 \times 10^{21} \text{ cm}^{-2}$, $N(\text{H}_2) = 4 \times 10^{20} \text{ cm}^{-2}$ and $N(\text{H}_2) = 3 \times 10^{21} \text{ cm}^{-2}$ in the red, central and blue part of the flows respectively. We assume that the flow has a depth of 0.07 pc, yielding volume densities $n(\text{H}_2) = 6 \times 10^3 \text{ cm}^{-3}$, $n(\text{H}_2) = 2 \times 10^3 \text{ cm}^{-3}$ and $n(\text{H}_2) = 1 \times 10^4 \text{ cm}^{-3}$ in the same regions. Parise et al. (2008) estimate $T = 30 - 50 \text{ K}$ from CO and methanol observations. In our modeling we use $T = 40 \text{ K}$. We estimate the *ortho*-water abundances to $(0.1 - 1) \times 10^{-5}$ in the outflow and 2×10^{-4} at the central position. However, Parise et al. (2008) give a density of $n(\text{H}_2) = 1 \times 10^5 \text{ cm}^{-3}$ in the region. Using this higher value we obtain *ortho*-water abundances of $(2 - 6) \times 10^{-7}$ in the outflow and 3×10^{-6} towards the central source. The emission has broader wings in the central position, a feature present also in the SWAS data. The origin of this high velocity component and the elevated water abundance might be the smaller outflow originating from IRS 2,

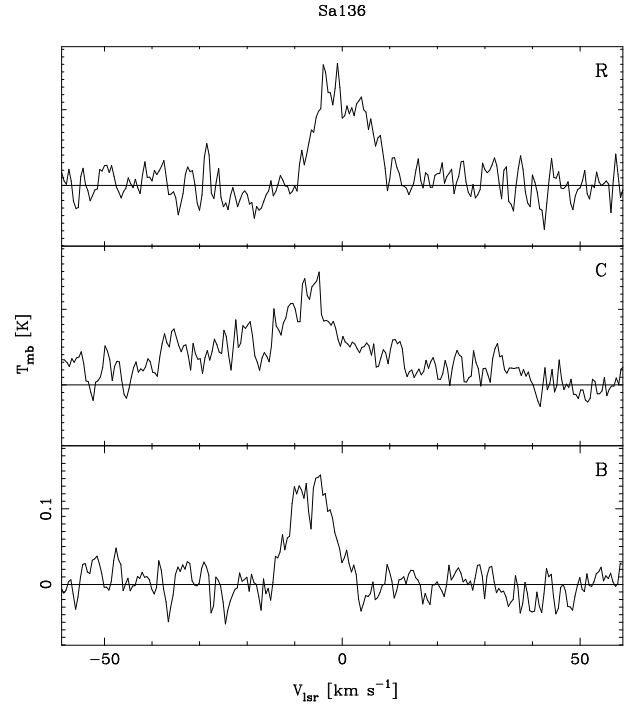


Fig. 5. The same as Figure 3 but for Sa136.

visible in Figure 4. Based on the outflow mass ($1.3 M_{\odot}$), dynamical time scale ($1 \times 10^4 \text{ yr}$) and flow velocity (28 km s^{-1}) provided by Bourke et al. (1997)⁴ for the larger flows, we estimate the mass loss rate to be $\dot{M}_{\text{loss}} = 3.6 \times 10^{-5} M_{\odot} \text{ yr}^{-1}$. The wind velocity is assumed to be 100 km s^{-1} .

4.2.7. HH54 B

The Herbig-Haro object HH54 B is situated in the Cha II cloud at roughly 200 pc (Hughes & Hartigan 1992). During the observations, the correlator suffered from ripple. This had the effect of increasing the line intensity and a substantial amount of data had to be abandoned. The signal detected can therefore only be classified as tentative although we are confident that the data do not show any systematic variations. Complementary data were obtained in CO(3-2), CO(2-1), SiO(5-4), SiO(3-2) and SiO(2-1) with the SEST telescope (see Appendix A) and in CO(5-4) with Odin. The CO(5-4) data suffer from frequency drift, something that puts an $\sim 10 \text{ km s}^{-1}$ uncertainty to our velocity scale. However, we do not believe that this gives large uncertainties on the line strength.

No shock-enhanced emission was detected in any of the observed SiO transitions. This result seems not easily reconcilable with the prediction from theoretical C-shock models (see Fig. 6 of Gusdorf et al. 2008), which appear closely adaptable to the conditions in HH 54 (Liseau et al. 1996; Neufeld et al. 2006).

Both the CO(2-1) and (3-2) lines show an absorption feature at $+2.4 \text{ km s}^{-1}$, which corresponds to the LSR-velocity of the molecular cloud. In addition, a strong blue wing is observed in all positions, but essentially no redshifted gas, which is in agreement with the (1-0) observations by Knee (1992). Both (2-1) and (3-2) transitions peak at the central map position, i.e. on HH 54B itself and their integrated intensities, $\int T_{\text{A}}^* dv$, are given in Table A.1.

⁴ These authors estimate t_d to 10 700 years and 10 200 years for the south east and the north west lobe respectively.

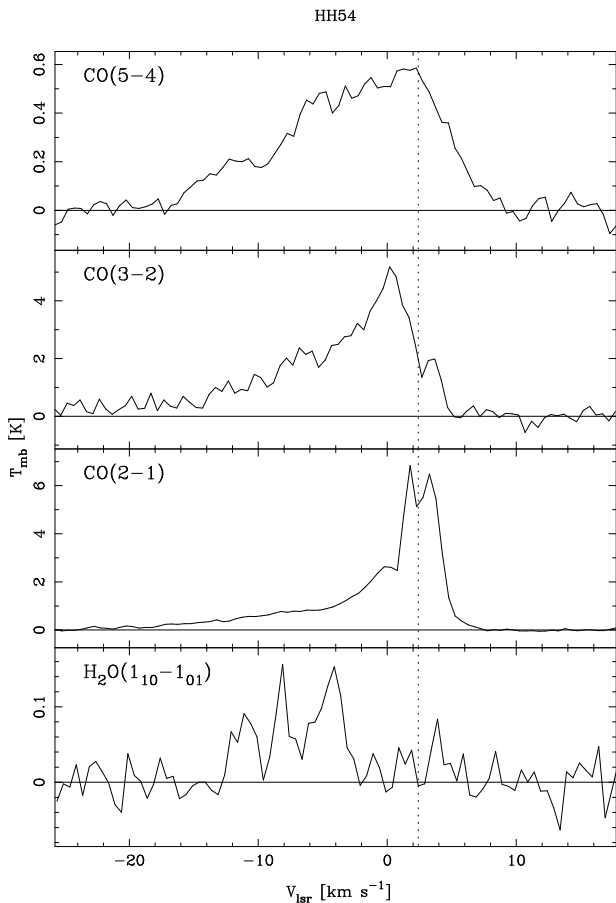


Fig. 6. From top to bottom the CO(5-4), CO(3-2), CO(2-1) and H₂O(1₁₀ – 1₀₁) spectra observed towards HH54 B are plotted. The dotted vertical line shows the cloud LSR-velocity at +2.4 km s⁻¹.

For the comparison with the ISO-LWS model of Liseau et al. (1996), we use the average radiation temperature, approximated by $\langle T \rangle = \eta_{\text{mb}}^{-1} \int T_{\text{A}}^* dv / \int dv$. This yields $\langle T_{21} \rangle = (1.2 \pm 0.02)$ K and $\langle T_{32} \rangle = (3.2 \pm 0.33)$ K for the CO (2-1) and (3-2) lines, respectively. Both values are smaller, by 25% and 40% respectively, than the model predictions of 1.6 K and 5.7 K, which were based on a single-temperature approximation. Even though the strength of the CO(5-4) line is uncertain, it shows a slightly higher temperature than the predicted 0.3 K. Putting it all together, the model predicts the radiation temperature in all three lines to within an order of 2. For the RADEX analysis we use the ISO-LWS model $T = 330$ K, $n(\text{H}_2) = 2 \times 10^5 \text{ cm}^{-3}$ and $N(\text{H}_2) = 3 \times 10^{19} \text{ cm}^{-2}$, where the column density has been diluted to the Odin beam. We obtain a beam averaged water abundance of $X(o\text{-H}_2\text{O}) = 3 \times 10^{-6}$. However, recently Neufeld et al. (2006) estimate a higher H₂ column density for the warm gas, a fact that could alter our derived abundance by an order of magnitude downwards. The mass loss rate of the unknown driving source has been estimated by Giannini et al. (2006) as $\dot{M}_{\text{loss}} = 3 \times 10^{-6} M_{\odot} \text{ yr}^{-1}$.

4.2.8. G327.3-0.6

The hot core G327.3-0.6 is located in the southern hemisphere at the distance of 2.9 kpc (Bergman 1992). CO line profiles obtained by Wyrowski et al. (2006) weakly indicate the presence of outflows, however, to date there is no further study of this. From CO observations performed by these authors, we infer $N(\text{H}_2)$

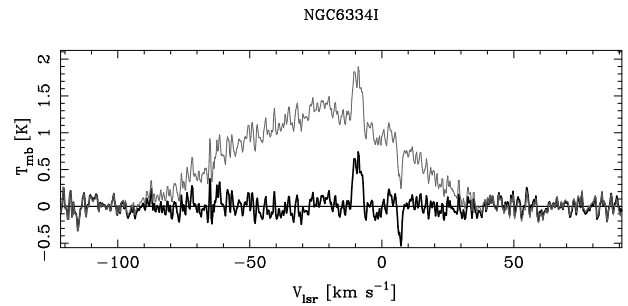


Fig. 7. The same as Figure 3 but for NGC6334 I. The black spectrum represents the first case and the grey spectrum represents the second case as described in Section 4.2.9

$= 2 \times 10^{22} \text{ cm}^{-2}$ and $n(\text{H}_2) = 4 \times 10^5 \text{ cm}^{-3}$, assuming $[^{18}\text{CO}/\text{H}_2] = 10^{-7}$ and a source size 25". The volume density inferred is slightly lower than the range 10^6 – 10^8 cm^{-3} given by Bergman (1992), who also estimates the temperature to be within the range of 40 – 200 K. Using a value of 100 K gives an upper limit of $X(o\text{-H}_2\text{O}) < 8 \times 10^{-10}$. A temperature of 40 K will increase the inferred upper limit by a factor of 8.

4.2.9. NGC6334 I

At least two outflows are emerging from NGC6334 I, located in the constellation Scorpius (McCutcheon et al. 2000) at the distance of 1.7 kpc (Neckel 1978). From CO observations provided by Leurini et al. (2006) we obtain a beam averaged column density $1 \times 10^{20} \text{ cm}^{-2}$ and a volume density $4 \times 10^3 \text{ cm}^{-3}$. We assume that the gas temperature is the same as the dust temperature, viz. $T = 100$ K (Sandell 2000). This is consistent with Leurini et al. (2006) who set a lower limit on the kinetic temperature at 50 K. With the above properties we derive an abundance of $X(o\text{-H}_2\text{O}) = 5 \times 10^{-5}$.

The baseline subtracted spectrum does not show any evidence of high velocity gas. However, we do not find this easily reconcilable with the high velocity gas detected in several CO transitions by Leurini et al. (2006). One possibility could be the curved baseline hiding the outflow wings. Therefore, we investigate also an alternative case where we assume that the entire curvature stems from the outflowing gas. This secondary scenario is perhaps not very likely. However, at present it is not possible to draw any firm conclusions. The estimated depth of the absorption feature is greater than the continuum level of 360 Jy, interpolated from 800 μm observations provided by Sandell (2000). In this secondary case we derive the abundance $X(o\text{-H}_2\text{O}) = 2 \times 10^{-3}$.

4.2.10. Ser SMM1

The Serpens star forming dark cloud is situated in the inner Galaxy at a distance of 310 pc (de Lara et al. 1991). Franklin et al. (2008) estimated *ortho*-water abundances of $X(o\text{-H}_2\text{O}) = 7.1 \times 10^{-7}$ and $X(o\text{-H}_2\text{O}) = 3.8 \times 10^{-7}$ in the blue and red wing respectively while Larsson et al. (2002) estimate the water abundance to $X(\text{H}_2\text{O}) = 1 \times 10^{-5}$ in the region. Davis et al. (1999) provide the mass and size of the outflow based on CO observations. Assuming a width of 0.2 pc yields $n(\text{H}_2) = 1 \times 10^3 \text{ cm}^{-3}$ and $N(\text{H}_2) = 5 \times 10^{20} \text{ cm}^{-2}$. From OI(63 μm) measurements carried out by Larsson et al. (2002, and references therein) we obtain the mass loss rate, $\dot{M}_{\text{loss}} = 3 \times 10^{-7} M_{\odot} \text{ yr}^{-1}$. The temperature of the dust was constrained by White et al. (1995) to be 30 K

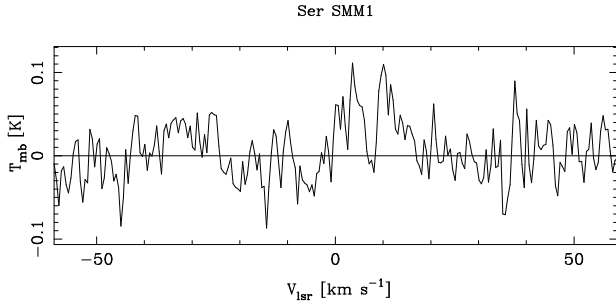


Fig. 8. The same as Figure 3 but for Ser SMM1.

$< T < 40$ K. Using $T = 35$ K and the above properties we obtain $X(o\text{-H}_2\text{O}) = 9 \times 10^{-5}$ and $X(o\text{-H}_2\text{O}) = 5 \times 10^{-5}$ in the blue and red flow.

4.2.11. B335

The dense core in the B335 globule is believed to be one of the major candidates for protostellar collapse. This isolated source at the distance of 150 pc (Stutz et al. 2008) harbors several Herbig-Haro objects associated with a bipolar outflow (see e.g. Galfalk & Olofsson 2007). Following the outflow mass estimate of $0.44 M_{\odot}$ in Hirano et al. (1988) we derive $n(\text{H}_2) = 1 \times 10^3 \text{ cm}^{-3}$ and $N(\text{H}_2) = 3 \times 10^{20} \text{ cm}^{-2}$. The size of the outflow is taken to be $2' \times 8'$. Based on the same mass, a dynamical time scale (2.3×10^4 yr) and a flow velocity (13 km s^{-1}), provided by these authors we derive $\dot{M}_{\text{loss}} = 2.5 \times 10^{-6} M_{\odot}$. The velocity of the wind is assumed to be 100 km s^{-1} . In our modeling we use a kinetic temperature of 20 K. This is an intermediate value in the modeling carried out by Evans et al. (2005, their Figure 8) who give the temperature as a function of radius for the inner 0.1 pc region. The derived upper limit of the water abundance is, $X(o\text{-H}_2\text{O}) < 1 \times 10^{-3}$. The rms implies a water abundance, $X(o\text{-H}_2\text{O}) < \sim 10^{-7}$ according to the infall model presented by Hartstein & Liseau (1998). Ashby et al. (2000) estimate the upper limit on the *ortho*-water abundance to be within the range $1.3 \times 10^{-7} - 7 \times 10^{-6}$.

4.2.12. L1157

L1157 is a Class 0 object in the constellation of Cepheus situated at the distance of 250 pc (Looney et al. 2007). It drives a prototype bipolar outflow which was observed by Odin in four different positions. The mass loss rate can be derived from mass ($0.62 M_{\odot}$) and time scale (15 000 yr) estimations given by Bachiller et al. (2001). Assuming a maximum CO velocity of 20 km s^{-1} and a stellar wind velocity of 100 km s^{-1} , we derive $\dot{M}_{\text{loss}} = 8.3 \times 10^{-6} M_{\odot} \text{ yr}^{-1}$. The Odin strip map covers the bulk of the outflow with two pointings in the red wing, one in the blue, and one on the driving source of the outflow itself (Figure 9). The observations were carried out using the AOS and the AC2 simultaneously. The spectra shown in Figure 10 are the averages of the merged data. The total mass in the different parts of the flow were obtained from CO observations carried out by Bachiller et al. (2001). From this we estimate $n(\text{H}_2) = 2 \times 10^3 \text{ cm}^{-3}$ and $N(\text{H}_2) = 2 \times 10^{20} \text{ cm}^{-2}$ in the northern lobe, while $n(\text{H}_2) = 3 \times 10^3 \text{ cm}^{-3}$ and $N(\text{H}_2) = 2 \times 10^{20} \text{ cm}^{-2}$ in the central and southern region. The size of the CO outflow is taken to be $50'' \times 375''$. For all four positions we set the kinetic temperature to $T = 30$ K, a rough global estimate based on Bachiller et al. (2001). We calculate the abundances in the outflow to be within the range of 2×10^{-4} and 1×10^{-3} . The

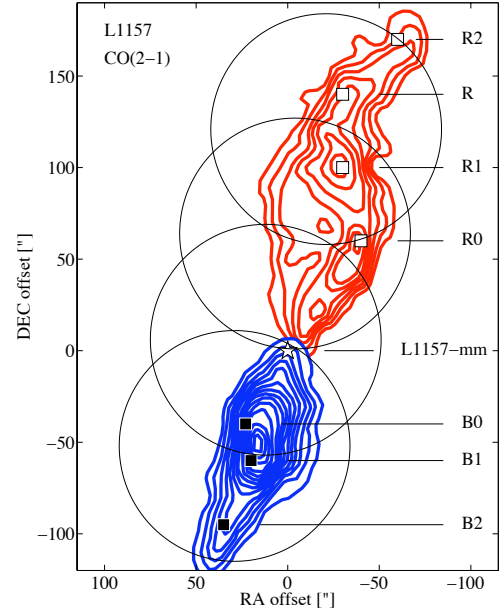


Fig. 9. The four positions observed by Odin are shown overlaid on a CO (2-1) map of L1157 (Bachiller et al. 2001). The circles correspond to the Odin beam at 557 GHz. Coordinate offsets are given with respect to L1157-mm, indicated in the figure with a star symbol: $\alpha_{2000} = 20:39:06.4$, $\delta_{2000} = +68:02:13.0$. The black and white squares refer to the knots B0, B1, B2, R0, R1, R and R2 described in Bachiller et al. (2001).

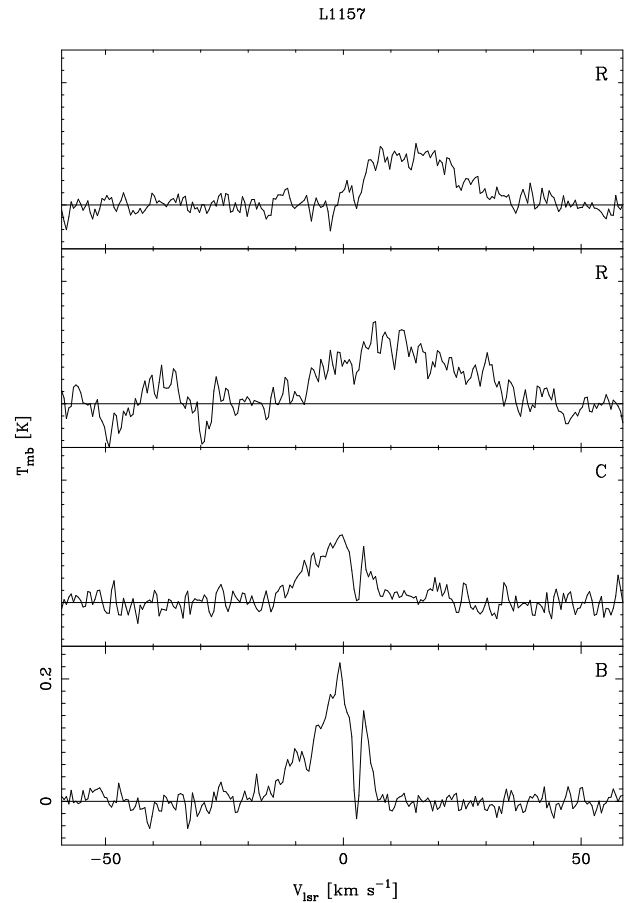


Fig. 10. The same as Figure 3 but for L1157.

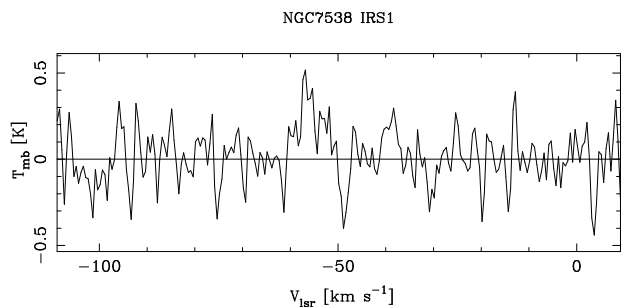


Fig. 11. The same as Figure 3 but for NGC7538 IRS1.

derived water abundance in the central region is slightly lower, $X(o\text{-H}_2\text{O}) = 2 \times 10^{-4}$ in the blue lobe and $X(o\text{-H}_2\text{O}) = 3 \times 10^{-5}$ in the red. The increased blue emission likely originates from the outflow. Within the Odin beam are the positions B0 and B1 that show peaked emission in H_2CO , CS, CH_3OH , SO (Bachiller et al. 2001, their Figure 1) and SiO (Nisini et al. 2007). Franklin et al. (2008) estimated $X(o\text{-H}_2\text{O}) = 8.0 \times 10^{-6}$ and $X(o\text{-H}_2\text{O}) = 9.7 \times 10^{-6}$ in the blue and red wing respectively.

Bachiller et al. (2001) estimates the density around the protostar to be $\sim 10^6 \text{ cm}^{-3}$. When moving from B0 to B2, the density changes from ~ 3 to $6 \times 10^5 \text{ cm}^{-3}$. Using $n(\text{H}_2) = 1 \times 10^6 \text{ cm}^{-3}$ and $n(\text{H}_2) = 5 \times 10^5 \text{ cm}^{-3}$ for the central and southern part respectively we obtain the abundances $X(o\text{-H}_2\text{O}) = 5 \times 10^{-7}$ and $X(o\text{-H}_2\text{O}) = 2 \times 10^{-6}$.

4.2.13. NGC7538 IRS1

NGC7538 IRS1 is a region of ongoing high mass star formation. The main infrared source IRS1 is located at the boundary of an HII region in the Perseus arm, located at a distance of 2.7 kpc (Moscadelli et al. 2008). In addition to IRS1, and its high velocity outflow, also several other sub-mm sources fall into the large Odin beam. The mass loss rate from IRS1 was estimated by Kameya et al. (1989) to be $\dot{M}_{\text{loss}} = 1 \times 10^{-4} M_{\odot} \text{ yr}^{-1}$. The total mass and size of this region is given by the same authors, yielding a volume density and column density of $n(\text{H}_2) = 3 \times 10^3 \text{ cm}^{-3}$ and $N(\text{H}_2) = 4 \times 10^{20} \text{ cm}^{-2}$ respectively. The kinetic temperature is assumed to be the same as the dust temperature, i.e. $T = 40$ (Sandell & Sievers 2004). We infer a limit to the water abundance of $X(o\text{-H}_2\text{O}) < 1 \times 10^{-4}$.

4.2.14. Supernova remnants

3C391 BML is a supernova remnant at the distance of 8 kpc (Chen & Slane 2001). The temperature, volume density and column density of the gas were constrained to $50 \text{ K} \leq T \leq 125 \text{ K}$, $10^4 \text{ cm}^{-3} \leq n(\text{H}_2) \leq 5 \times 10^5 \text{ cm}^{-3}$ and $N(\text{H}_2) \geq 4 \times 10^{20} \text{ cm}^{-2}$ from OH 1720 MHz maser observations carried out by Lockett et al. (1999). Using the lowest values for the temperature and volume density we calculate an upper limit of $X(o\text{-H}_2\text{O}) < 4 \times 10^{-6}$.

IC443 is a shell type supernova remnant at the distance of about 1.5 kpc (Fesen 1984). The broad emission peaks are labeled A through H, where Odin has observed clump G. The volume density and temperature were modeled by van Dishoeck et al. (1993) as $n(\text{H}_2) = 5 \times 10^5 \text{ cm}^{-3}$ and $T = 100 \text{ K}$. Using the CO column density inferred by the same authors, assuming a $[\text{CO}/\text{H}_2]$ ratio of 10^{-4} and a source size of $40'' \times 100''$, we obtain $N(\text{H}_2) = 3 \times 10^{21} \text{ cm}^{-2}$. The derived abundance is $X(o\text{-H}_2\text{O}) = 4 \times 10^{-8}$. This is in agreement with Snell et al. (2005) who derive an $o\text{-H}_2\text{O}$ abundance with respect to ^{12}CO , $X(o\text{-H}_2\text{O}) = 3.7 \times 10^{-4}$.

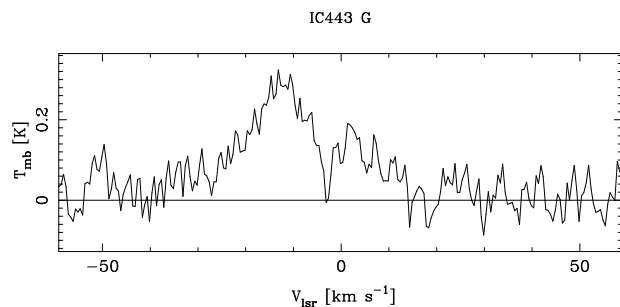


Fig. 12. The same as Figure 3 but for IC443-G.

4.3. Water abundance

The water abundances inferred from our analysis are given with respect to the molecular column density within the Odin beam. The values span a wide range with most of the sources having an abundance of the order 10^{-5} – 10^{-4} . The highest abundances in our sample are found in the outflows of L1157 and L1448. Supposing that the assumed physical properties are correct, we see an increased abundance in both the blue and the red wing of L1157. The derived water abundances are significantly low in G327.3-0.6. The reason for this is the combination of the high H_2 column density and temperature used. The water emission is also very likely beam diluted due to the large distance, resulting in lower beam averaged $o\text{-H}_2\text{O}$ abundances.

Assuming an inclination angle of 60° with respect to the line of sight for all the targets we plot the $o\text{-H}_2\text{O}$ abundances versus the maximum velocities (Figure 13). The maximum velocities are taken from the spectra as the maximum offsets between the cloud velocity and the flow velocity. There is a correlation between the derived abundances and the maximum velocities of the outflowing gas. The solid line in Figure 13 is the first order polynomial least square fit:

$$X(o\text{-H}_2\text{O}) = 10^{-7} v_{\text{max}}^2. \quad (2)$$

The correlation coefficient is 0.57 while the p-value, testing the hypothesis of no correlation is 0.04. Following the C-shock modelling carried out by Kaufman & Neufeld (1996), a relationship is expected when shocks are responsible for the emission. However, the abundances do not show any tendency to level off with velocities larger than $\sim 20 \text{ km s}^{-1}$ as shown in their Figure 3. This is an indication of a lack of J-type dissociative shocks in this sample of outflows. There are however uncertainties in our simplified analysis, for example the inclination of the outflow lobes and the RADEX analysis. The dependence between the water abundance and the maximum velocity is consistent with the analysis made by Franklin et al. (2008), although their method is based on binning the weak outflow lines into intervals of 5 km s^{-1} . We also plot the *ortho*-water abundances versus mass loss rates in Figure 14. G.327-0.6 is not included due to the lack of observations towards the assumed outflow, neither is NGC6334 I included in Figure 13 - 14 due to the curvature in the baseline. No obvious relationship can be picked out. The absence of a correlation is surprising inasmuch as high mass loss rates affect the budget of material available for water formation.

4.4. Comparison with SWAS data

The gas volume density, used as an input parameter to RADEX, has for all the outflows except TW Hya been derived from CO observations. This method generally underestimates the mass of

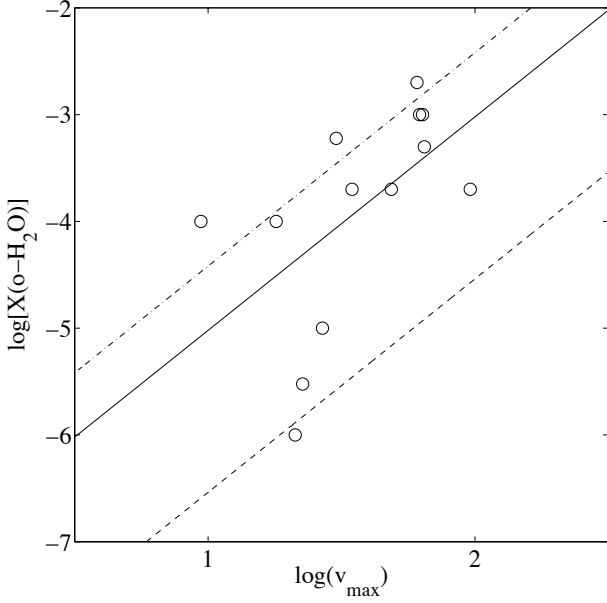


Fig. 13. o -H₂O abundance plotted against the maximum velocity for an overall inclination of 60° with respect to the line of sight. The solid line represents a linear fit of $\log[X(o\text{-H}_2\text{O})]$ versus $\log(v_{\max})$ with the same inclination angle applied. The dotted dashed line represents the fit with a inclination correction of 35° while the dashed line represents the fit with an inclination angle correction of 85°. The errorbars from the measurements are smaller than the circles.

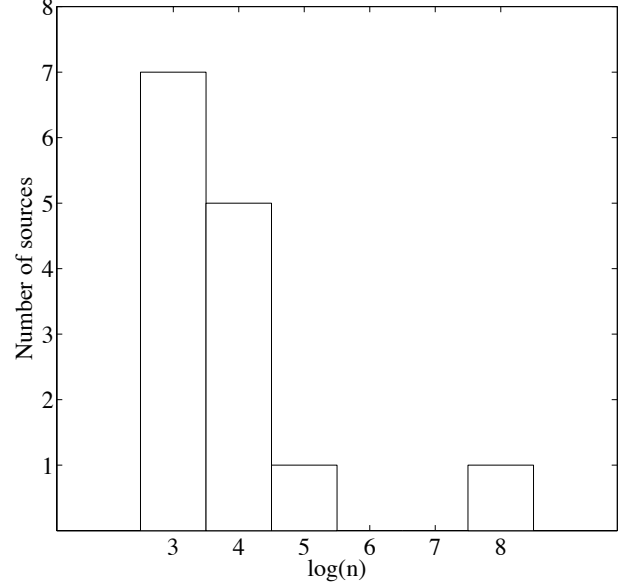


Fig. 15. A histogram of the gas volume density estimated in the outflows studied in this paper shows a variation that spans over six orders of magnitude.

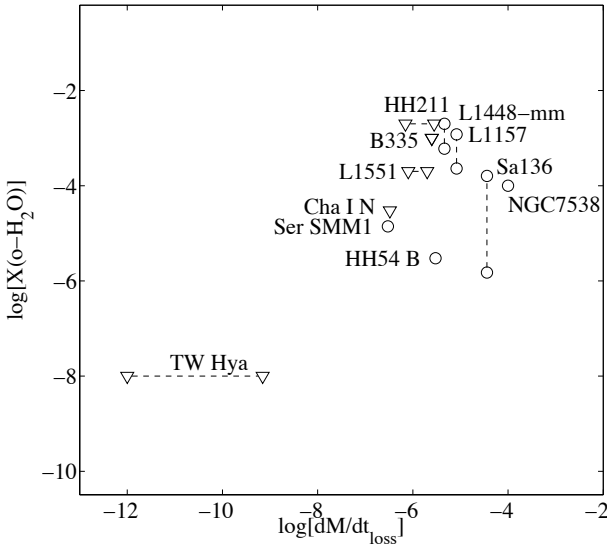


Fig. 14. o -H₂O abundance plotted against the mass loss rate. The triangles represent the high upper limits for each source on the o -H₂O abundance, while the circles symbolize values where a detection has been made. Dashed lines represent the cases where there is a range in the inferred abundances or mass loss rates.

the regions. The possibility that the water emission is originating from gas with a higher volume density than this can therefore not be ruled out. Nevertheless, we are confident that the volume density is actually spanning over a wide range of values. This is also one of the reasons why several of our derived abundances deviate from those inferred by Franklin et al. (2008). They use a single volume density of $n(\text{H}_2) = 10^5 \text{ cm}^{-3}$ and our values differ from this by more than two orders of magnitude for some of the sources (see Table 2). Figure 15 shows a histogram of the num-

bers of sources within different volume density ranges. The difficulty to estimate the gas column density of the water emitting regions is a problem that has to be addressed in order to interpret the future observations with Herschel.

The integrated intensities for the SWAS and Odin outflow spectra are compared in Figure 16 to provide an estimate of the source size of the water emitting regions. The dashed 1:1 ratio line illustrates the case where the source is filling both antenna beams while the dashed 3.37:1 line is indicating a small source size compared to both beams. Assuming that both the emitting sources and the antenna responses are circularly symmetric and Gaussian, these ratios follow from the relation:

$$\frac{I_{\text{Odin}}}{I_{\text{SWAS}}} = \frac{(3.3 \times 60 \times 4.5 \times 60) + \theta^2}{126^2 + \theta^2}, \quad (3)$$

where θ is source size. The SWAS spectra have been retrieved from the SWAS spectrum server and baseline subtracted. The integrated intensities are measured in the same regions as for the Odin spectra and the spectra chosen for comparison are those where the pointing is equal or within a smaller fraction of a beam. We can conclude that the sources are filling a large fraction of the beam for Ser SMM1, L1157 and NGC 7538 1. On the other hand, the source sizes are small for HH54 B and L1448.

4.5. Outflows and observed water abundances

The main objective for these observations was to use the ground state o -H₂O transition as a tracer for shocked gas. Available shock models by Bergin et al. (1998) show that a shock velocity in excess of 10 km s^{-1} should convert essentially all oxygen, not in the form of CO, into water resulting in water abundances relative to H₂ of the order 10^{-4} . This water is also believed to persist for $\sim 10^5$ years. For several of our sources, the water abundance increases as high as what would be theoretically possible for these C-type shocks. The fact that we are observing abundances as high as this, might be an indication that the shock velocities are in this regime. On the other hand, the large Odin beam does not show whether the water emission regions are small or not.

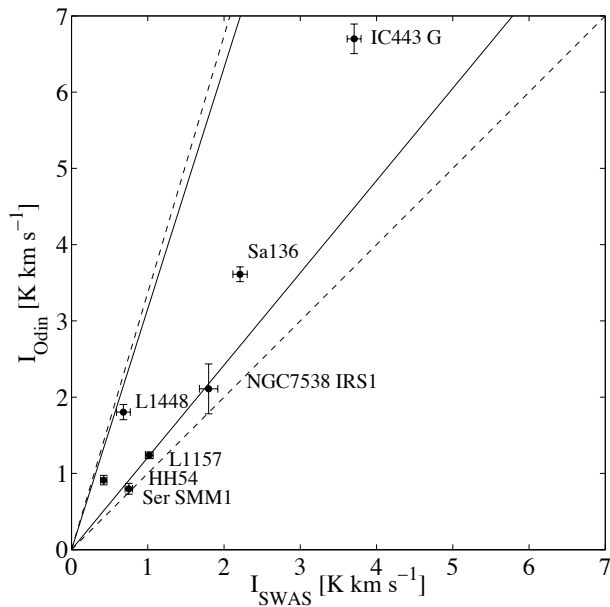


Fig. 16. Integrated intensities for common sources of Odin and SWAS. The dashed lines show the 3.37:1 and the 1:1 ratios between the Odin and SWAS integrated intensities. The error bars refer to the analysis and the solid lines represents ratios 1:1 and 3.37:1 with a 15 % uncertainty applied. This is the estimated error limit from the data reduction.

The density in these regions may also very well be orders of magnitude higher than the values used in this paper, a fact that could alter our inferred values significantly. Future observations with the *Herschel space observatory* will give us the ability to spatially resolve outflows and it will also give us the possibility to observe several different transitions originating in gas of different temperatures. This will hopefully give a much deeper insight into the chemistry occurring in these structures.

5. Conclusions

We make the following primary conclusions:

1. We have observed 13 outflows and two supernova remnants and detect the *ortho*-water ground state rotational transition in seven outflows and one super-nova remnant.
2. The column densities of *o*-H₂O have been investigated with RADEX, having the volume density, temperature, line intensity and linewidth as input. Elevated abundances of water are found in several sources. The abundances are as high as one would expect if all gaseous oxygen had been converted to water in a C-type shock.
3. There is no distinct relationship between the water abundance and the mass loss rate.
4. There is a correlation between the *o*-H₂O abundance and the maximum velocity of the gas.

Acknowledgments. The author enjoyed interesting discussions with John H. Black concerning radiative transfer in general and RADEX in particular. Carina M. Persson and Per Bergman are also greatly acknowledged. We thank the Research Councils and Space Agencies in Sweden, Canada, Finland and France for their financial support. The valuable comments made by the anonymous referee are highly appreciated.

Table 2. Column densities of *o*-H₂O and estimates of the *ortho*-water abundance, $X(o\text{-H}_2\text{O}) = N(o\text{-H}_2\text{O})/N(\text{H}_2)$. The offsets are the reconstructed pointing offsets and the numbers in the parentheses are the 1σ statistical uncertainties. Upper limits are 3σ .

Source	Offset (", ")	$\int T_{\text{mb}}(\text{H}_2\text{O})dv$ (K km s ⁻¹)	Δv (km s ⁻¹)	$N(\text{H}_2)$ (10 ¹⁹ cm ⁻²)	T_{kin} (K)	Method 1			Method 2			
						$n(\text{H}_2)$ (10 ³ cm ⁻³)	$N(o\text{-H}_2\text{O})$ (10 ¹⁵ cm ⁻²)	$X(o\text{-H}_2\text{O})$ (10 ⁻⁵)	$n(\text{H}_2)$ (10 ³ cm ⁻³)	$N(o\text{-H}_2\text{O})$ (10 ¹⁵ cm ⁻²)	$X(o\text{-H}_2\text{O})$ (10 ⁻⁵)	
Odin sources analyzed in this paper:												
L1448	(-38, +69)	0.53 (0.63)	-10 → 7	6	37	1	37	60	10	7	10	10
	(+2, -2)	1.80 (0.10)	-8 → 29	6	37	1	91	100	10	19	30	30
	(+32, -81)	1.19 (0.07)	8 → 35	6	37	1	102	200	10	20	30	30
HH 211	(-47, +4)	< 1.01		4	12	10	< 56	< 200				
	(+14, -21)	< 0.56		4	12	10	< 30	< 80				
	(+73, -46)	< 0.96		4	12	10	< 53	< 100				
L1551	(+84, +18)	< 1.29		100	20	3	< 79	< 8				
	(-129, -194)	< 1.43		100	20	3	< 88	< 9				
	(-342, -404)	< 2.36		100	20	3	< 159	< 20				
IC443-G	(-2, -28)	6.70 (0.19)	-39 → 15	300	100	500	0.09	0.004				
TW Hya ^a	(-16, +5)	< 0.014		0.3	40	1000	< 0.00003	< 0.001				
ε Cha I N	(+42, -24)	< 1.071		39	50	2	< 10	< 3				
Sal36	(-46, +146)	1.62 (0.06)	-11 → 10	130	40	6	13	1	100	0.8	0.06	0.06
	(-16, -4)	4.03 (0.10)	-52 → 40	38	40	2	74	20	100	1	0.3	0.3
	(+13, -154)	1.35 (0.05)	-16 → 3	280	40	13	4	0.1	100	0.5	0.02	0.02
HH54 B	(+2, +5)	0.91 (0.06)	-15 → 5	3	330	200	0.09	0.3				
G327.3-0.6	(-1, -21)	< 1.56		2360	100	4	< 0.02	< 0.00008				
NGC6334I,												
Case 1	(+13, -33)	2.23 (0.15)	-13 → -5	10	100	4	5	5				
NGC6334I,												
Case 2	(+13, -33)	96.0 (0.6)	-93 → 36	10	100	4	235	200				
Ser SMM1	(-3, +8)	0.36 (0.05)	-1 → 8	50	35	1	48	9				
		0.43 (0.05)	8 → 17	50	35	1	23	5				
		< 0.82		40	50	10	< 2	< 0.4				
3C391 BML ^b	(+1, -7)	< 1.62		27	20	1	< 337	< 100				
B335	(+3, -36)	0.08 (0.02)	-2 → 3	16	30	2	5	3				
L1157	(-21, +121)	1.75 (0.05)	3 → 36	16	30	2	88	60				
		0.71 (0.06)	-16 → 2	16	30	2	38	20				
	(-4, +64)	2.33 (0.08)	2 → 38	16	30	2	180	100				
	(+12, +6)	1.03 (0.04)	-15 → 3	20	30	3	34	20				
	(+29, -52)	0.21 (0.02)	3 → 8	20	30	3	7	3	1000	0.08	0.04	0.04
		1.83 (0.04)	-21 → 3	23	30	3	53	20	1000	0.02	0.008	0.008
		0.29 (0.02)	3 → 8	23	30	3	9	4	500	0.3	0.1	0.1
NGC7538 IRS 1	(+26, -4)	2.11 (0.33)	-62 → -50	39	40	3	51	10	500	0.05	0.02	0.02

Notes to the Table: ^a The volume density and column density are inferred from HCN and H₂ observations. ^b The volume density and column density are inferred from OH 1720 MHz maser observations.

References

- Ashby, M. L. N., Bergin, E. A., Plume, R., et al. 2000, *ApJ*, 539, L119
- Bachiller, R., Guilloteau, S., Dutrey, A., Planesas, P., & Martin-Pintado, J. 1995, *A&A*, 299, 857
- Bachiller, R., Guilloteau, S., & Kahane, C. 1987, *A&A*, 173, 324
- Bachiller, R., Martin-Pintado, J., Tafalla, M., Cernicharo, J., & Lazareff, B. 1990, *A&A*, 231, 174
- Bachiller, R., Pérez Gutiérrez, M., Kumar, M. S. N., & Tafalla, M. 2001, *A&A*, 372, 899
- Benedettini, M., Viti, S., Giannini, T., et al. 2002, *A&A*, 395, 657
- Bergin, E. A., Neufeld, D. A., & Melnick, G. J. 1998, *ApJ*, 499, 777
- Bergman, P. 1992, PhD thesis, Göteborg, Sweden, (1992)
- Bourke, T. L. 2001, *ApJ*, 554, L91
- Bourke, T. L., Garay, G., Lehtinen, K. K., et al. 1997, *ApJ*, 476, 781
- Ceccarelli, C., Haas, M. R., Hollenbach, D. J., & Rudolph, A. L. 1997, *ApJ*, 476, 771
- Chen, Y. & Slane, P. O. 2001, *ApJ*, 563, 202
- Davis, C. J., Matthews, H. E., Ray, T. P., Dent, W. R. F., & Richer, J. S. 1999, *MNRAS*, 309, 141
- de la Reza, R., Jilinski, E., & Ortega, V. G. 2006, *AJ*, 131, 2609
- de Lara, E., Chavarría-K., C., & Lopez-Molina, G. 1991, *A&A*, 243, 139
- Dickman, R. L. 1978, *ApJS*, 37, 407
- Dubernet, M.-L., Daniel, F., Grosjean, A., & Lin, C. Y. 2009, *A&A*, 497, 911
- Dubernet, M.-L. & Grosjean, A. 2002, *A&A*, 390, 793
- Dupree, A. K., Brickhouse, N. S., Smith, G. H., & Strader, J. 2005, *ApJ*, 625, L131
- Enoch, M. L., Young, K. E., Glenn, J., et al. 2006, *ApJ*, 638, 293
- Evans, II, N. J., Lee, J.-E., Rawlings, J. M. C., & Choi, M. 2005, *ApJ*, 626, 919
- Faure, A., Crimier, N., Ceccarelli, C., et al. 2007, *A&A*, 472, 1029
- Fesen, R. A. 1984, *ApJ*, 281, 658
- Franklin, J., Snell, R. L., Kaufman, M. J., et al. 2008, *ApJ*, 674, 1015
- Frisk, U., Hagström, M., Ala-Laurinaho, J., et al. 2003, *A&A*, 402, L27
- Gålfalk, M. & Olofsson, G. 2007, *A&A*, 475, 281
- Giannini, T., McCoe, C., Nisini, B., et al. 2006, *A&A*, 459, 821
- Gueth, F. & Guilloteau, S. 1999, *A&A*, 343, 571
- Gusdorf, A., Cabrit, S., Flower, D. R., & Pineau Des Forêts, G. 2008, *A&A*, 482, 809
- Hartstein, D. & Liseau, R. 1998, *A&A*, 332, 703
- Henning, T., Pfau, W., Zinnecker, H., & Prusti, T. 1993, *A&A*, 276, 129
- Herbig, G. H. 1998, *ApJ*, 497, 736
- Herczeg, G. J., Wood, B. E., Linsky, J. L., Valenti, J. A., & Johns-Krull, C. M. 2004, *ApJ*, 607, 369
- Hirano, N., Kameya, O., Nakayama, M., & Takakubo, K. 1988, *ApJ*, 327, L69
- Hjalmarson, Å., Frisk, U., Olberg, M., et al. 2003, *A&A*, 402, L39
- Hughes, J. & Hartigan, P. 1992, *AJ*, 104, 680
- Kameya, O., Hasegawa, T. I., Hirano, N., Takakubo, K., & Seki, M. 1989, *ApJ*, 339, 222
- Kastner, J. H., Zuckerman, B., Weintraub, D. A., & Forveille, T. 1997, *Science*, 277, 67
- Kaufman, M. J. & Neufeld, D. A. 1996, *ApJ*, 456, 611
- Kenyon, S. J., Dobrzycka, D., & Hartmann, L. 1994, *AJ*, 108, 1872
- Kessler, M. F., Steinz, J. A., Anderegg, M. E., et al. 1996, *A&A*, 315, L27
- Klotz, A., Harju, J., Ristorcelli, I., et al. 2008, *A&A*, 488, 559
- Knee, L. B. G. 1992, *A&A*, 259, 283
- Knude, J. & Hog, E. 1998, *A&A*, 338, 897
- Lamzin, S. A., Kravtsova, A. S., Romanova, M. M., & Batalha, C. 2004, *Astronomy Letters*, 30, 413
- Larsson, B., Liseau, R., & Men'shchikov, A. B. 2002, *A&A*, 386, 1055
- Lee, C.-F., Ho, P. T. P., Palau, A., et al. 2007, *ApJ*, 670, 1188
- Leurini, S., Schilke, P., Parise, B., et al. 2006, *A&A*, 454, L83
- Linke, R. A., Goldsmith, P. F., Wannier, P. G., Wilson, R. W., & Penzias, A. A. 1977, *ApJ*, 214, 50
- Liseau, R., Ceccarelli, C., Larsson, B., et al. 1996, *A&A*, 315, L181
- Liseau, R., Fridlund, C. V. M., & Larsson, B. 2005, *ApJ*, 619, 959
- Liseau, R. & Olofsson, G. 1999, *A&A*, 343, L83
- Lockett, P., Gauthier, E., & Elitzur, M. 1999, *ApJ*, 511, 235
- Looney, L. W., Tobin, J. J., & Kwon, W. 2007, *ApJ*, 670, L131
- Mattila, K., Liljeström, T., & Toriseva, M. 1989, in *Low Mass Star Formation and Pre-main Sequence Objects*, ed. B. Reipurth, 153–171
- McCutcheon, W. H., Sandell, G., Matthews, H. E., et al. 2000, *MNRAS*, 316, 152
- Melnick, G. J., Stauffer, J. R., Ashby, M. L. N., et al. 2000, *ApJ*, 539, L77
- Moscadelli, L., Reid, M. J., Menten, K. M., et al. 2008, *ArXiv e-prints*
- Neckel, T. 1978, *A&A*, 69, 51
- Neufeld, D. A., Melnick, G. J., Sonnentrucker, P., et al. 2006, *ApJ*, 649, 816
- Nisini, B., Codella, C., Giannini, T., et al. 2007, *A&A*, 462, 163
- Nordh, H. L., von Schéele, F., Frisk, U., et al. 2003, *A&A*, 402, L21
- Olberg, M., Frisk, U., Lecacheux, A., et al. 2003, *A&A*, 402, L35
- Olofsson, A. O. H., Olofsson, G., Hjalmarson, Å., et al. 2003, *A&A*, 402, L47
- Parise, B., Belloche, A., Leurini, S., & Schilke, P. 2008, *Ap&SS*, 313, 73
- Parise, B., Belloche, A., Leurini, S., et al. 2006, *A&A*, 454, L79
- Persson, C. M., Olberg, M., Hjalmarson, Å., et al. 2009, *A&A*, 494, 637
- Phillips, T. R., Maluendes, S., & Green, S. 1996, *ApJS*, 107, 467
- Qi, C., Wilner, D. J., Aikawa, Y., Blake, G. A., & Hogerheijde, M. R. 2008, *ApJ*, 681, 1396
- Ristorcelli, I., Falgarone, E., Schöier, F., et al. 2005, in *IAU Symposium*, Vol. 235, *IAU Symposium*, 227P–+
- Sandell, G. 2000, *A&A*, 358, 242
- Sandell, G. & Sievers, A. 2004, *ApJ*, 600, 269
- Sandqvist, A. 1977, *A&A*, 57, 467
- Snell, R. L., Hollenbach, D., Howe, J. E., et al. 2005, *ApJ*, 620, 758
- Snell, R. L., Howe, J. E., Ashby, M. L. N., et al. 2000, *ApJ*, 539, L93
- Snell, R. L., Loren, R. B., & Plambeck, R. L. 1980, *ApJ*, 239, L17
- Stojimirović, I., Narayanan, G., Snell, R. L., & Bally, J. 2006, *ApJ*, 649, 280
- Stutz, A. M., Rubin, M., Werner, M. W., et al. 2008, *ApJ*, 687, 389
- Ulich, B. L. & Haas, R. W. 1976, *ApJS*, 30, 247
- van der Tak, F. F. S., Black, J. H., Schöier, F. L., Jansen, D. J., & van Dishoeck, E. F. 2007, *A&A*, 468, 627
- van Dishoeck, E. F., Jansen, D. J., & Phillips, T. G. 1993, *A&A*, 279, 541
- van Zadelhoff, G.-J., van Dishoeck, E. F., Thi, W.-F., & Blake, G. A. 2001, *A&A*, 377, 566
- Werner, M. W., Roellig, T. L., Low, F. J., et al. 2004, *ApJS*, 154, 1
- White, G. J., Casali, M. M., & Eiroa, C. 1995, *A&A*, 298, 594
- Wilson, C. D., Mason, A., Gregersen, E., et al. 2003, *A&A*, 402, L59
- Wyrowski, F., Menten, K. M., Schilke, P., et al. 2006, *A&A*, 454, L91

Table 3. Column densities of *o*-H₂O and estimates of the *ortho*-water abundance, $X(o\text{-H}_2\text{O}) = N(o\text{-H}_2\text{O})/N(\text{H}_2)$.

Source	Offset (" , ")	$\int T_{\text{mb}}(\text{H}_2\text{O})dv$ (K km s ⁻¹)	Δv	$N(\text{H}_2)$ (10 ¹⁹ cm ⁻²)	$N(o\text{-H}_2\text{O})$ (10 ¹⁵ cm ⁻²)	$X(o\text{-H}_2\text{O})$ (10 ⁻⁷)
Odin sources analyzed by other authors:						
W3 ^a	(0, 0)	3.9 (0.1)				0.02
Orion KL ^b	(0, 0)	323			400	80 / 1000
	(+0, -240)	24			0.09	0.1
Cha-MMS1 ^c	(+18, -21)					< 0.07
	(-35, +32)					< 0.07
IRAS 16293-2422 ^d	(+68, -50)		red wing			30
			blue wing			11
	(+31, -10)		red wing			600
			blue wing			60
	(-23, -8)		red wing			130
			blue wing			11
S140 ^e	(0, 0)					0.05 – 4
VLA1623 ^f	(0, 0)		red wing	2	0.2 – 0.4	100 – 200

Notes to the Table: ^a Wilson et al. (2003). The offset is with respect to $\alpha_{2000} = 02:25:40.6$, $\delta_{2000} = +62:05:57$. ^b Olofsson et al. (2003). These authors use two different values for $N(\text{H}_2)$ towards the (0, 0) position. The offsets are with respect to $\alpha_{2000} = 05:35:14.4$, $\delta_{2000} = -05:22:30$. ^c Klotz et al. (2008). The offsets are with respect to $\alpha_{2000} = 11:06:31.7$, $\delta_{2000} = -77:23:32$. ^d Ristorcelli et al. (2005); Ristorcelli, private communication. The offsets are with respect to $\alpha_{2000} = 16:32:23.0$, $\delta_{2000} = -24:28:40$. ^e Persson et al. (2009), towards the PDR and the outflow. The offset is with respect to $\alpha_{2000} = 22:19:19.4$, $\delta_{2000} = +63:18:50$. ^f Larsson et al. in prep, private communication. The offset is with respect to $\alpha_{2000} = 16:23:20.2$, $\delta_{2000} = -24:22:55$.

Appendix A: Ground based observations

The observations with the Swedish ESO Submillimetre Telescope (SEST) were made during 11-20 August 1997 and 2-6 August 1998. Some complementary SiO (2-1) map data were collected during 7-9 February 2003. The observed molecules and their transitions are listed in Table A.1 and for SiO (2-1) and (3-2), the observations were done simultaneously.

SIS receivers were used as frontends and the backend was a 2×1 GHz multi-channel acousto-optical spectrometer (AOS), split into two halves for the SiO (2-1) and (3-2) observations. For the SiO (5-4) and the CO observations, both the high resolution (HRS) and the low resolution (LRS) backends were used. The channel separation of the HRS was 43 kHz and the spectral resolution 80 kHz covering the bandwidth of 86 MHz, corresponding to $\delta v = 0.07$ km s⁻¹ and $\Delta v = \pm 35$ km s⁻¹ for the velocity resolution and range at 345 GHz, respectively. For the LRS, these parameters were channel separation 0.69 MHz and $\Delta v = 1.4$ MHz spectral resolution, providing $\delta v = 1.2$ km s⁻¹ and $\Delta v = \pm 700$ km s⁻¹, respectively, for the CO (3-2) observations.

The data were chopper-wheel calibrated in the T_{A}^* -scale (Ulich & Haas 1976) and the main beam efficiencies at the different frequencies, η_{mb} , are given in Table A.1. The pointing of the telescope was regularly checked towards point sources, masing in the SiO ($v=1$, $J=2-1$) line, and was determined to be better than 3'' (rms). However, for HH 54, all SiO data refer to the vibrational ground state, $v=0$, and the (2-1) and (3-2) data were obtained in frequency switching mode, with a frequency chop of 4 MHz.

Knee (1992) assigned a kinetic gas temperature of ~ 15 K to the bulk cloud material. In the CO (3-2) line, this should yield a high contrast between the cloud and the high velocity gas. To achieve flat, optimum baselines, the CO (3-2) observations were done therefore in wide dual beam switching with throws of $\pm 11'$ in azimuth. At this maximum amplitude available at the SEST, the reference beams were still inside the molecular cloud. For

this reason, this mode could not be adopted for the CO (2-1) observations, which were performed in total power mode. The reference position was 1° north of HH 54. Centered on the object, nine point maps with 25'' spacings were obtained in both CO lines. In addition, a tighter sampled nine point map with 15'' spacings was also made in CO (3-2).

Table A.1. Molecular line observations with the 15 m SEST

Transition	Frequency (MHz)	HPBW ($''$)	η_{mb}	T_{sys} (K)	T_{rms} (mK)	Backend	Δv_{lsr} (km s $^{-1}$)	$\int T_{\text{A}}^* dv$ (K km s $^{-1}$)
CO (2-1)	230538.0	23	0.50	500	95/10	HRS/LRS	-26.3 to -0.3	15.6 \pm 0.3
CO (3-2)	345796.0	15	0.25	1600	470/70	HRS/LRS	-16.4 to +0.8	13.6 \pm 1.4
SiO (2-1)	86846.9	58	0.75	160	10 ^a	HRS		
SiO (3-2)	130268.7	38	0.68	190	15 ^a	HRS		
SiO (5-4)	217104.9	23	0.61	750	35/7 ^a	HRS/LRS		

Note to the Table: ^a This is the rms of the average spectrum, including all positions.

Appendix B: Online material

For comparison we show the calibrated rawdata together with the baseline subtracted and smoothed spectra already shown in the text.

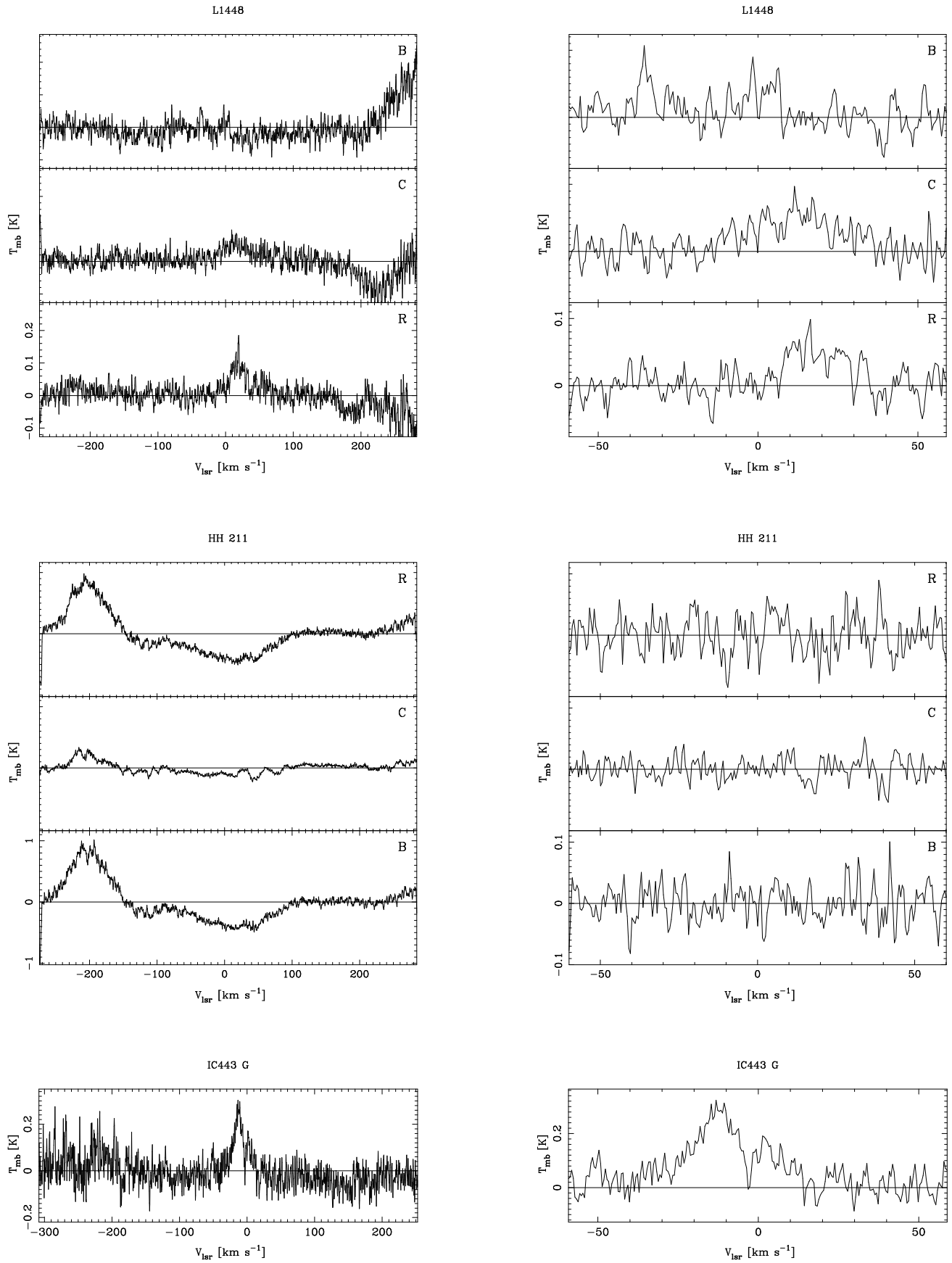


Fig. B.1. This figure shows the L1448, HH211 and IC443-G spectra. The positions are listed in Table 1. All spectra on the right are smoothed to a resolution of 0.5 km s^{-1} and clipped for clarity. These spectra are also calibrated in frequency. The spectra on the left are the calibrated rawdata with a zero order baseline subtraction. For strip maps, a letter in the upper right corner indicates in which part of the flow the spectra has been collected (R=red, B=blue and C=center).

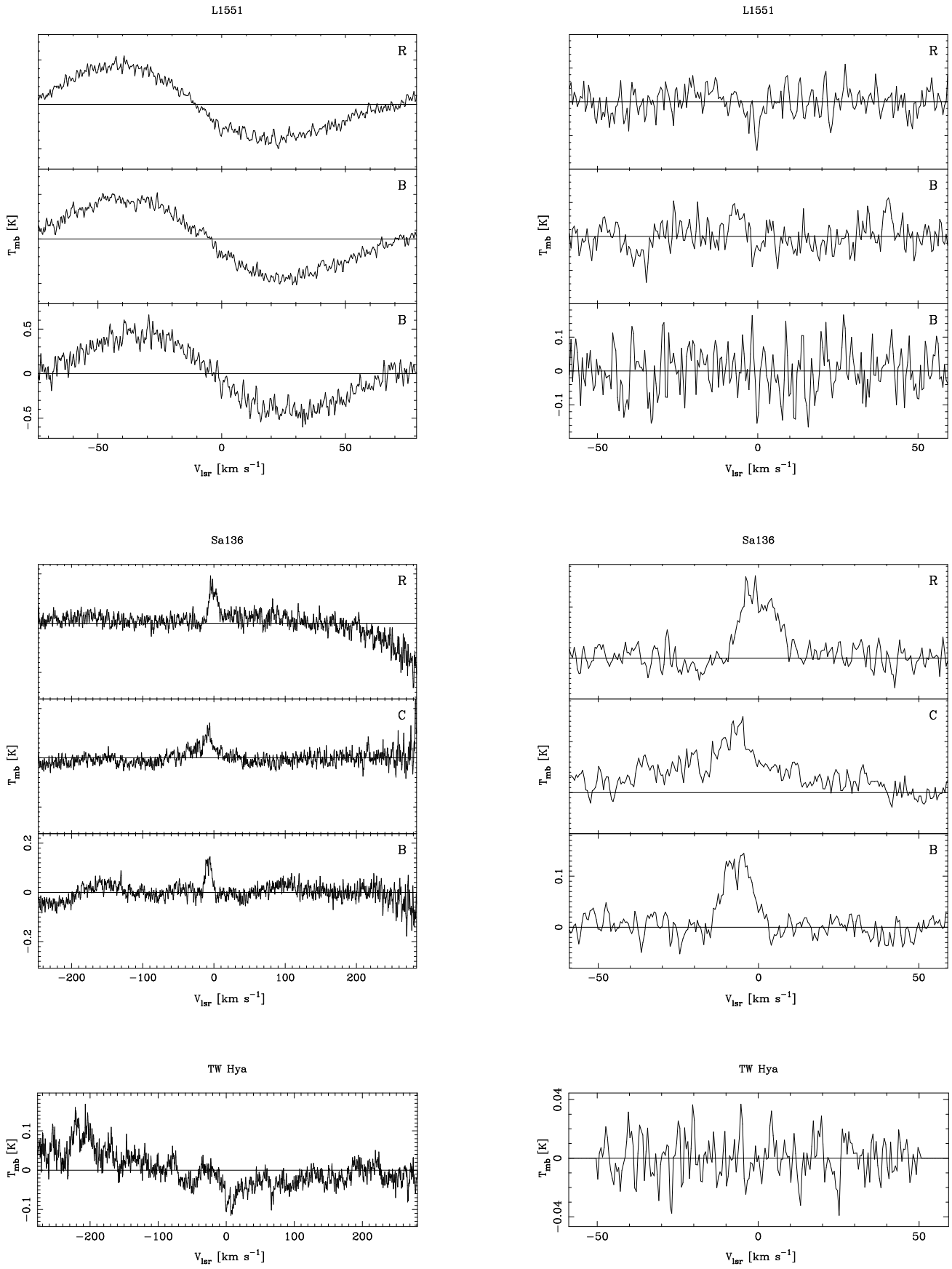


Fig. B.2. The same as Figure B.1 but for L1551, Sa136 and TW Hya.

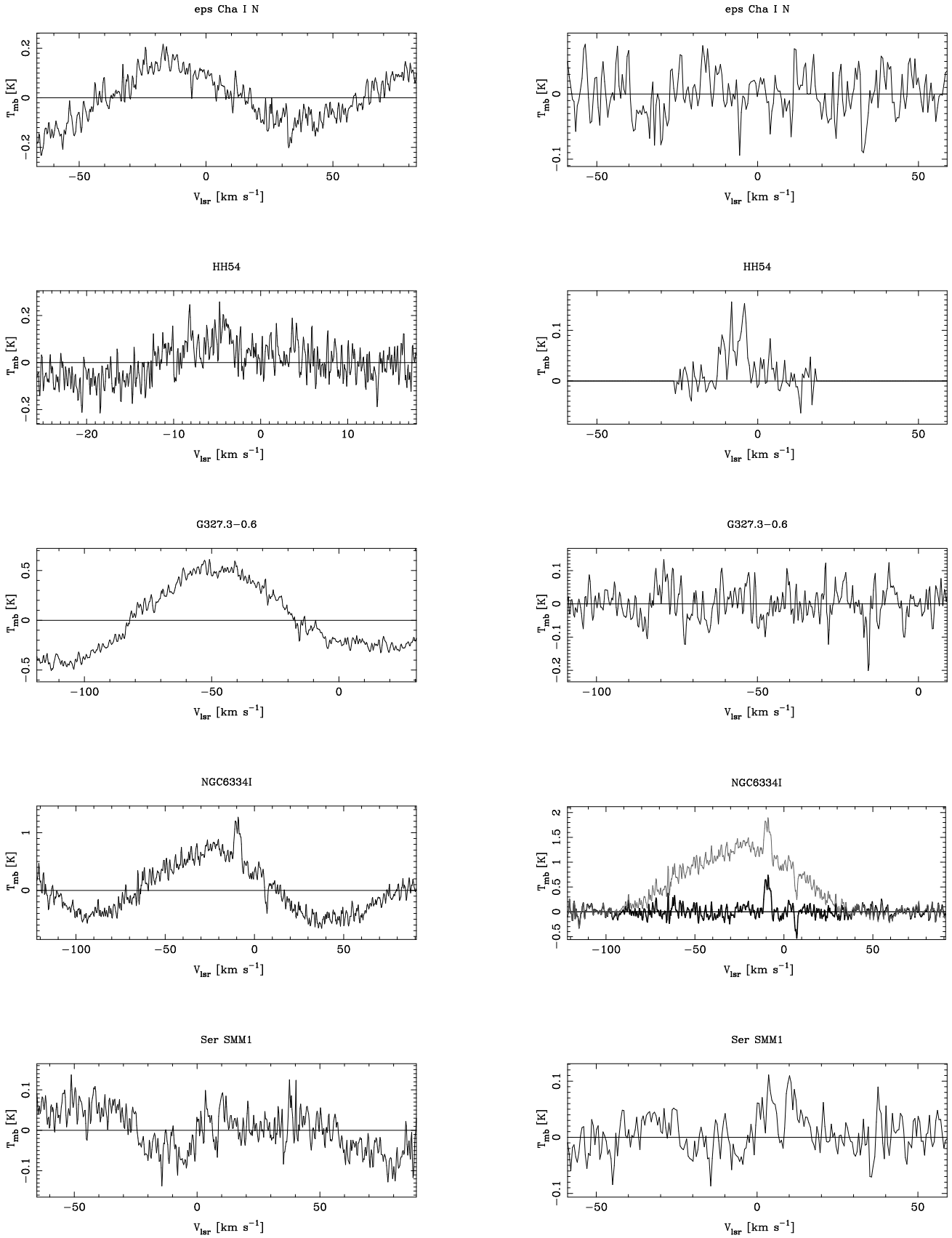


Fig. B.3. The same as Figure B.1 but for eps Cha I N, HH54 B, G327.3-0.6, NGC6334I and Ser SMM1.

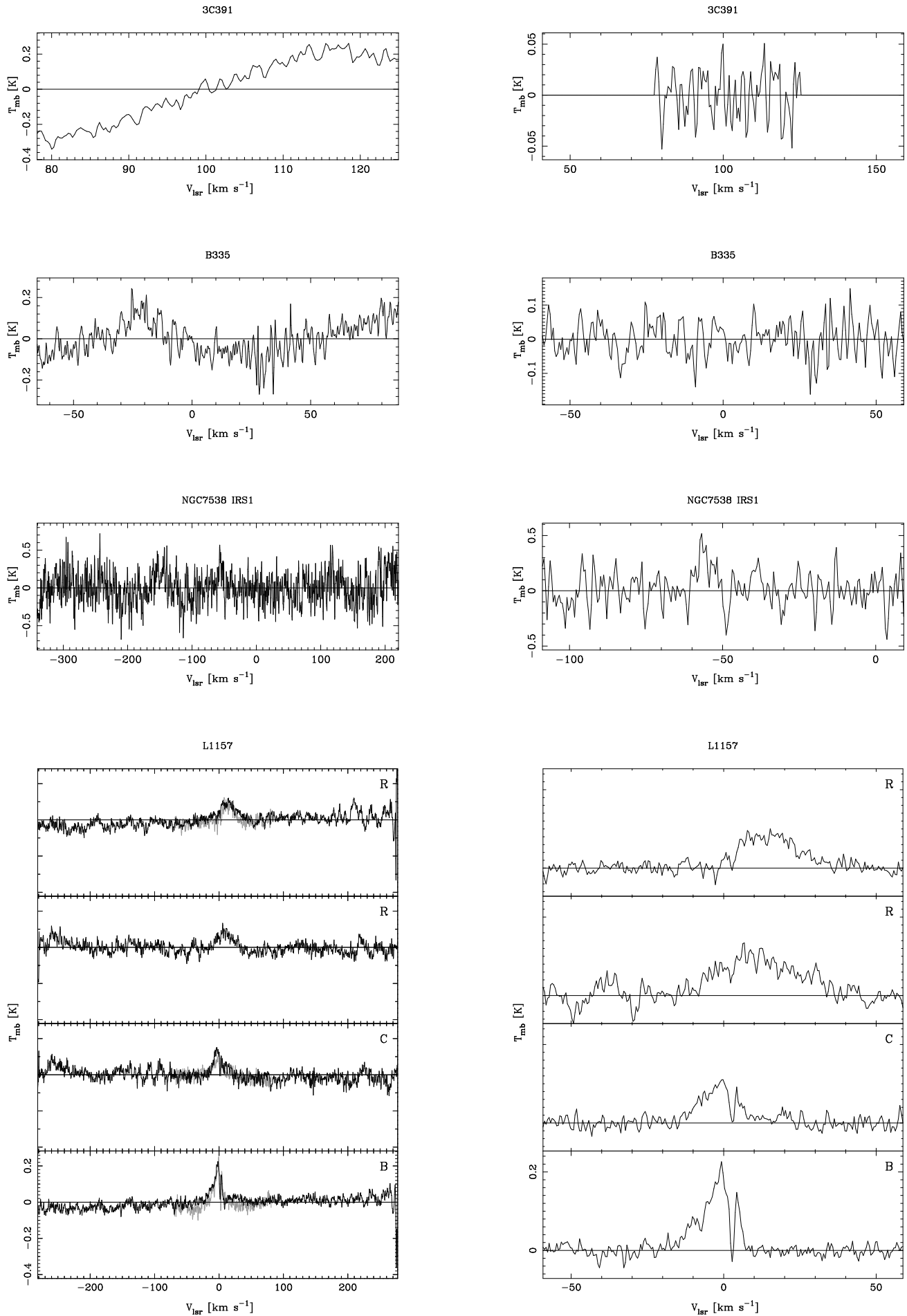


Fig. B.4. The same as Figure B.1 but for 3C391 BML, B335, NGC7538 IRS1 and L1157. For L1157, the AC2 data are plotted in gray and the AOS data in black.